ACS SENSORS

pubs.acs.org/acssensors Article

Understanding the Increasing Trend of Sensor Signal with Decreasing Oxygen Partial Pressure by a Sensing-Reaction Model Based on O^{2-} Species

Liupeng Zhao, Xueqin Gong, Wei Tao, Tianshuang Wang, Peng Sun,* Fangmeng Liu, Xishuang Liang, Fengmin Liu, Yanchao Wang, and Geyu Lu*

Cite This: *ACS Sens.* 2022, 7, 1095−1104 Read Online

ACCESS | Metrics & More | Article Recommendations | Supporting Information

ABSTRACT: Although the increasing trend of sensor signal with decreasing oxygen partial pressure was observed quite early, the underlying mechanism is still elusive, which is a hindrance to accurate gas detection under varying oxygen partial pressure. In this work, a sensing model based on previous experimental and theoretical results is proposed, in which the O^{2-} species is determined to be the main oxygen species because O^- species has not been observed by direct spectroscopic studies. On this basis, combined with the band bending of SnO_2 at different oxygen partial pressures, the functional relationship between the surface electron concentration, oxygen partial pressure, and reducing gas concentration is established, which includes three forms corresponding to the depletion layer, accumulation layer, and flat band. In the depletion layer case, the variation of the sensor resistance to different concentrations of CO and oxygen can be well fitted with our function model. Besides, this model predicts that the response of sensors will no longer maintain the increasing trend in an extremely hypoxic atmosphere but will decrease and approach 1 with the background oxygen content further going down to 0.

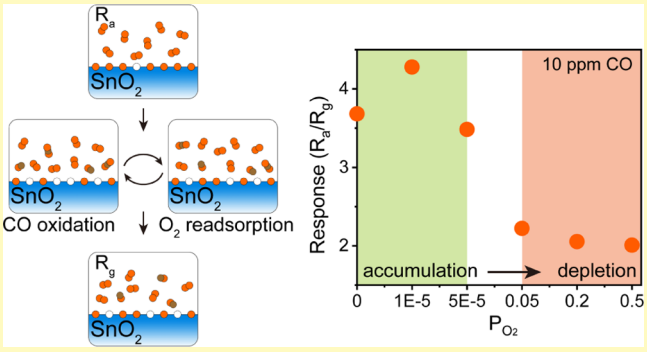

KEYWORDS: *SnO_2 gas sensor, sensing model, background oxygen partial pressure, mechanism, O^{2-} species*

Semiconductor metal oxides, especially SnO_2, have a long history of application in gas sensors, primarily due to their high sensitivity in a wide range of flammable and toxic gases.[1−6] The basic sensing mechanism is the reduction−oxidation reaction on the surface that causes electron transfer and results in a change in resistance.[7,8] Therefore, the oxygen partial pressure in the background atmosphere plays a central role in gas detection, which enables the sensors to exhibit a high baseline resistance by oxygen adsorption and provides active oxygen species for subsequent sensing reactions. However, early studies found that the response of SnO_2-based sensors to propane increased with decreasing oxygen partial pressure, and the response reached the maximum value in the absence of oxygen (actually, there was still a background oxygen of 50 ppm for "0% O_2").[9] Further experiments revealed that this phenomenon was also observed for other reducing gases.[10] Recently, with increasing demand for gas sensors in traditional and emerging fields, it is inevitable that there will be a variation of oxygen partial pressure in the application environment. For example, the wide utilization of oxygen enrichment equipment due to the continuously decreasing cost of oxygen-enriched technology can reduce the ignition point and lower the flammability limits of flammable gases, which increase the risk of fire and explosion.[11] In addition, the promising non-invasive detection of diseases using volatile biomarkers in the exhaled breath also needs to consider the reduction of oxygen concentration in the exhalation (∼15% oxygen content in exhaled gases).[12]

Although the abnormal behavior that the response of SnO_2-based sensors to reducing gases decreases with the increase of oxygen partial pressure has been found a long time ago, the underlying reason is still unclear. For a SnO_2-based sensor, its resistance shows a decreasing trend with decreasing O_2 concentrations. In an oxygen-deficient atmosphere, the decrease in baseline resistance (R_a) and the increase in gas response (R_a/R_g, where R_g is the resistance in reducing gases) suggest a remarkable increase in surface charge transfer, which seems to be in contradiction with the reduction of adsorbed oxygen species on the surface. Therefore, in the beginning, this phenomenon was explained by the adsorption of the reducing

Received: December 30, 2021
Accepted: March 14, 2022
Published: March 29, 2022

Downloaded via JILIN UNIV on March 13, 2023 at 14:05:42 (UTC).
See https://pubs.acs.org/sharingguidelines for options on how to legitimately share published articles.

ACS Publications © 2022 American Chemical Society

https://doi.org/10.1021/acssensors.1c02753
ACS Sens. 2022, 7, 1095−1104

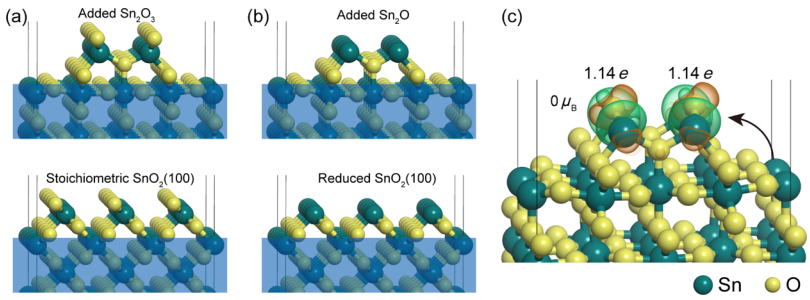

Figure 1. (a) Atomic arrangement of the reconstructed SnO_2(110) surface (the added Sn_2O_3 model) and the stoichiometric SnO_2(100) surface. (b) Atomic arrangement of the reconstructed SnO_2(110) surface (the added Sn_2O model) and the reduced SnO_2(100) surface. (c) Bader charges of adsorbed oxygen on the reconstructed SnO_2(110) surface (the green region represents charge depletion and the orange region represents charge accumulation).

gas itself. As a result, the electrons would be transferred directly from the reducing gas to the oxide.[9] However, further research found that some reducing gases such as CO cannot be adsorbed on the SnO_2 surface (the DRIFT spectra show no carbonyl species on pure SnO_2 samples), but such a phenomenon still existed.[13] The results suggest that the reaction between CO and ionosorbed oxygen would cause the CO sensitivity to decrease with the increase of oxygen partial pressure.

In this work, in order to understand the effect of oxygen partial pressure on the sensitivity of SnO_2-based sensors, a sensing model is proposed based on previous experimental and theoretical results. In this model, O^{2-} species is determined to be the main adsorbed oxygen species on the surface of SnO_2, which can react with reducing gases, leaving oxygen vacancies on the surface. The ionization of the additional oxygen vacancies leads to the decrease in resistance. However, due to the exceptional deep donor state of oxygen vacancies, there are some oxygen vacancies which cannot be ionized even at the working temperature. Based on this, the functional relationship between the surface electron concentration, oxygen partial pressure, and reducing gas concentration is established, which has three forms according to the band bending in different oxygen backgrounds. Combined with the measured resistance and response curves of the SnO_2-based sensor to CO gas under different oxygen partial pressures, it is found that the model can describe the change of CO response with the variation of oxygen partial pressure well. Furthermore, the model predicts that the CO response will reduce with the decrease of oxygen partial pressure in an extremely hypoxic atmosphere, which is further verified by experiments.

■ RESULTS AND DISCUSSION

Identifying Model Variables and Inter-relationships. For SnO_2-based gas sensors, the charge transfer takes place by two processes: oxygen dissociative adsorption (capturing electrons from SnO_2) and the oxidation of reducing gas (releasing electrons into SnO_2). Therefore, in order to model the effect of oxygen partial pressure on the sensitivity of SnO_2-based sensors, it is essential to understand the relationship between surface electrons (n_S), oxygen partial pressure (P_{O_2}), and reducing gas concentration.

Oxygen Adsorption. The oxygen adsorption has been studied and intensely discussed for decades.[14−17] First, it is generally accepted that oxygen cannot be exothermically adsorbed on the stoichiometric surface but prefers to be adsorbed on a reduced surface at bridging oxygen vacancy sites. Second, the adsorbed oxygen species on the SnO_2 surface are considered to have three forms: O_2^-, O^-, and O^{2-}. The superoxide (O_2^-) species was observed only after oxygen adsorption at T < 150 °C by the EPR study.[18] For the O^- species, with the development of characterization techniques and theoretical studies, a growing number of researchers have been questioning the existence of O^- species because this species has not been observed by direct spectroscopic studies.[18] Furthermore, by means of DFT calculations, Sopiha et al. built several relatively stable O^- adsorption configurations by adding one extra electron into the system (weak adsorption for the neutral charged surface).[19] However, the calculated magnetic moment for all configurations is 1 μ_B, which is inconsistent with the EPR experiment. Meanwhile, the DFT calculations indicate that none of the O^- adsorption configurations are stable with respect to the surface O_2^- adsorption configurations. Noteworthily, they found the only stable O^{2-} adsorption configuration on the SnO_2(100) surface with a magnetic moment of 0 μ_B (the nonmagnetic nature of O^{2-} explains why it is not visible to the EPR study), which meets all the characteristics of a true O^{2-} state. Again, the problem is obvious because this crystal plane is less exposed compared with SnO_2(110) or SnO_2(101) in practice.

However, the SnO_2 surface is strongly dependent on external conditions (e.g., temperature, pressure, oxygen partial pressure, and so forth.), causing the surface to be easily reconstructed.[20,21] Li et al. proposed the added Sn_2O model by using in situ Cs-corrected STEM.[21] Although the reconstruction of SnO_2(110) finally occurred at 800 °C in vacuum (~10^{-5} Pa), the SnO_x species begin to appear on the SnO_2(110) surface at 300−500 °C, which is consistent with the claimed O^- desorption temperature in the O_2-TPD experiment (one important evidence for the existence of O^-).[14] In addition, we find that the reconstructed SnO_2(110) surface has a similar atomic arrangement with the outermost layer of SnO_2(100), as shown in Figure 1a,b. Furthermore, the authors simulated the dissociative adsorption of oxygen and found that there is a very low oxygen dissociative barrier of only 0.36 eV and a strong dissociative adsorption energy of −3.36 eV. As for the unreconstructed SnO_2(110) surface, there is only weak physical adsorption for the O_2 molecule on the Sn^{4+} site with an adsorption energy of −0.04 eV. Based on the dissociative adsorption configuration, we calculated the Bader charges (Figure 1c) on the adsorbed oxygen (1.14e for each O adatom) and the corresponding magnetic moment (0 μ_B) which is the same as the O^{2-} species found on the SnO_2(100) surface by Sopiha et al. (Bader charge on the O adatom is 1.16e

https://doi.org/10.1021/acssensors.1c02753
ACS Sens. 2022, 7, 1095−1104

and its magnetic moment is 0 μ_B). The reconstruction of $SnO_2(110)$ indicates that O^{2-} species can be adsorbed on the $SnO_2(110)$ surface, not just on the $SnO_2(100)$ surface. Therefore, combined with the current experimental and theoretical studies on adsorbed oxygen, O^{2-} species is determined to be the dominant species on the $SnO_2(110)$ surface at the working temperature.

Sensing Reactions on the SnO_2 Surface. During the detection of reducing gases, the adsorbed oxygen will be consumed, leaving donor oxygen vacancies on the surface, which is clear because the reaction products can be easily detected.[22,23] Apart from this, it is necessary to consider the adsorption of the reducing gas itself and the adsorption of oxidation products and further to confirm whether charge transfer occurs during the process if such adsorption behaviors exist.[13] For the effect of the adsorption of reducing gas itself, although it can be confirmed by experiments that the reducing gas can be adsorbed on the SnO_2 surface, it is difficult to determine whether charge transfer occurs during the process because the oxidation of the reducing gas proceeds simultaneously, and it is impossible to distinguish the effect of these two behaviors on the resistance separately. Therefore, the contribution of the adsorption of reducing gas itself to the change of resistance is hard to obtain. For the effect of the adsorption of the oxidation products, the effect can be directly observed by exposing the sensor to an atmosphere containing the oxidation products. In this work, we focus on the reducing gases and oxidation products that cannot be adsorbed on the SnO_2 surface or the adsorptions can exist but have no effect on resistance. To this end, CO gas is selected to verify the rationality of the established model because CO gas is a currently known gas that cannot be adsorbed on the SnO_2 surface. The DRIFT spectra of the SnO_2 sample show no carbonyl species when exposed to 300 ppm CO.[24] Meanwhile, the oxidation product (CO_2) has no effect on resistance (Figure S1).[24]

Surface Electron Concentration. As a typical N-type oxide, the studies on the surface electron concentration can be attributed to the research on the surface donor defects, which took a long time of discussion to prove that oxygen vacancy is a shallow donor and is recognized as the major donors in SnO_2.[25−28] Furthermore, the oxygen vacancy is found to be doubly ionizable defect and rationalized by DFT calculations,[29] which demonstrate that the single ionization of V_O^+ is unstable in SnO_2 for all values of E_F in the band gap, and only doubly positive (V_O^{2+}) and neutral (V_O) defects can exist. Nevertheless, the oxygen vacancy donor state is rather deep, about 0.5 eV below the conduction band minimum in theory and 0.15 eV at ∼700 °C in the experiment,[27,29] which indicates that some oxygen vacancies cannot be ionized even at the working temperature.

Briefly, the experimental and theoretical bases of our model are as follows:

(i) O^{2-} is determined to be the main adsorbed oxygen species on the surface of SnO_2. The formation of O^{2-} requires the consumption of one oxygen vacancy and two electrons.

(ii) The ionization of the additional oxygen vacancies caused by CO oxidation leads to the decrease in resistance.[30,31]

(iii) The electrons in SnO_2 are generated by the secondary ionization of oxygen vacancies, and the oxygen vacancy is not fully ionized even at working temperatures.

Establishment of the Model. Based on the above discussion, the sensing reactions on the SnO_2 surface can be described as

$$\frac{1}{2}O_2(g) + 2e^- + V_O^{2+} \rightleftarrows O_O \tag{1}$$

$$CO(g) + O_O \rightarrow CO_2(g) + V_O \tag{2}$$

$$V_O \rightleftarrows V_O^{2+} + 2e^- \tag{3}$$

The rate equation for the adsorbed oxygen is

$$\frac{d[O_O]}{dt} = k_{ads}\cdot[V_O^{2+}]\cdot n_s^2\cdot P_{O_2}^{1/2} - k_{des}\cdot[O_O] - k_{react}\cdot P_{CO}\cdot[O_O] \tag{4}$$

where, k_{ads}, k_{des}, and k_{react} are the rate constants of oxygen adsorption, oxygen desorption, and CO oxidation, respectively. In the case of the steady state

$$k_{ads}\cdot[V_O^{2+}]\cdot n_s^2\cdot P_{O_2}^{1/2} = (k_{des} + k_{react}\cdot P_{CO})\cdot[O_O] \tag{5}$$

Notably, because the formation of O^{2-} requires the consumption of one oxygen vacancy and two electrons, the O^{2-} species can be considered as the impurity compensation for the oxygen vacancy rather than a new surface defect. Therefore, a significant difference from the previous model is that we are more interested in the variation of surface oxygen vacancies, precisely the concentration of ionized oxygen vacancies. According to eq 1, when oxygen vacancies are occupied by oxygen adsorption, eq 3 will shift to the right, which results in $|\Delta[O_O]|$ being greater than $|\Delta[V_O^{2+}]|$. Remember that the concentration of surface electrons depends on the number of ionized oxygen vacancies. Therefore, the space charge per unit area (Q_S) on the surface due to oxygen adsorption is not equal to $2q\Delta[O_O]$ but $-2q\cdot\Delta[V_O^{2+}]$. In different oxygen partial pressure, the energy bands would bend downward or upward, causing electrons to follow different distribution functions. Therefore, it is necessary to set an initial value to determine the change of the electron concentration. Here, the initial value is set in the case of a flat band, namely, the concentration of oxygen vacancies on the surface is the same as that in the bulk. In this case, the concentrations of oxygen vacancies (the sum of ionized $V_{O,ini}^{2+}$ and unionized $V_{O,ini}$ vacancies), lattice oxygen, and electrons on the surface are defined as $[V_{O,T}]$, $[O_{O,T}]$, and n_B, as shown in Figure 2.

During the oxygen adsorption and CO oxidation, the decrease of surface oxygen vacancies is equal to the increase of surface oxygen species

$$[O_O] - [O_{O,T}] = -([V_O^{2+}]\cdot n_S^2/K_i + [V_O^{2+}] - [V_{O,T}]) \tag{6}$$

where, K_i is the ionization equilibrium constant of oxygen vacancy. The space charge per unit area (Q_S) caused by the change of ionized oxygen vacancy is

$$Q_S = -2q([V_O^{2+}] - [V_{O,ini}^{2+}]) = q\int_0^\infty n_B(e^{\beta\varphi} - 1)\,dx \tag{7}$$

Using the Poisson equation and $\beta \equiv q/kT$ (k and T are the Boltzmann constant and temperature, respectively), one can obtain

https://doi.org/10.1021/acssensors.1c02753
ACS Sens. 2022, 7, 1095−1104

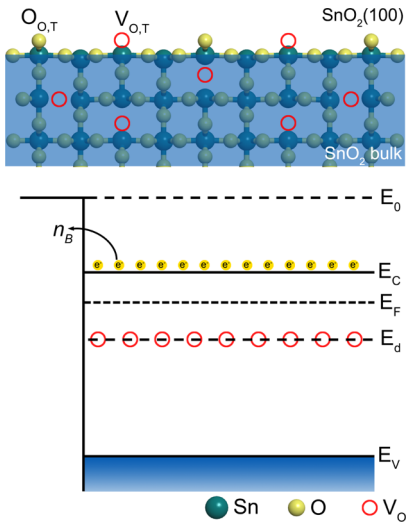

Figure 2. SnO_2 surface and bulk under flat-band conditions and the corresponding energy-band diagram.

$$Q_S = \mp\frac{\sqrt{2}\,\varepsilon_S}{\beta L_D}\sqrt{e^{\beta\varphi_S} - \beta\varphi_S - 1}, \qquad L_D = \sqrt{\frac{\varepsilon_S kT}{q^2 n_B}} \tag{8}$$

where ε_s, φ_S, and L_D are the permittivity of SnO_2, surface potential, and the Debye length, respectively. The detailed derivation can be found in Note S2 of the Supporting Information For N-type semiconductors, a typical variation of the space-charge density Q_S as a function of surface potential φ_S is shown in Figure 3.

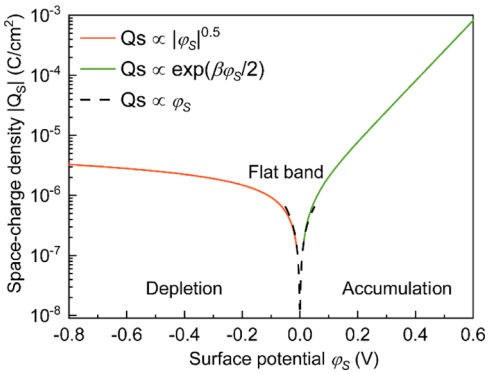

Figure 3. Variation of space charge density as a function of the surface potential φ_S for the SnO_2 semiconductor.

(i) For the depletion region case ($\varphi_S < 0$), the space-charge density Q_S is dominated by the second term in the root of eq 8, that is

$$Q_S \approx \frac{\sqrt{2}\,\varepsilon_S kT}{qL_D}\sqrt{-\beta\varphi} \propto \sqrt{|\varphi|} \tag{9}$$

(ii) For the accumulation region case ($\varphi_S > 0$), the space-charge density Q_S is dominated by the first term in the root of eq 8, that is

$$Q_S \approx -\frac{\sqrt{2}\,\varepsilon_S kT}{qL_D}e^{\beta\varphi_S/2} \propto e^{\beta\varphi_S/2} \tag{10}$$

(iii) In the region near the flat band $|\varphi| \ll 1/\beta$, using Taylor expansion $\lim_{\varphi\to 0}(e^{\beta\varphi} - 1) = \beta\varphi + (\beta\varphi)^2/2$, one can obtain

$$Q_S = \mp\frac{\varepsilon_s}{L_D}\varphi_S \propto \varphi_S \tag{11}$$

Equations 7 and 8 establish the relationship between oxygen vacancies (oxygen partial pressure) and band bending. However, in order to understand the effect of oxygen partial pressure on sensitivity, it is necessary to further confirm the relationship between the surface electron concentration and band bending. For the case of depletion layer, the distribution of electrons can be described by the Boltzmann distribution

$$n_S = n_B \exp(\beta\varphi_S) \tag{12}$$

By combining eqs 9 and 12, the space charge per unit area Q_S can be expressed by

$$Q_S = \sqrt{2\varepsilon_S kT\cdot n_B \ln\left(\frac{n_B}{n_S}\right)} \tag{13}$$

The relationship between n_S and the gas partial pressure (P_{O_2} and P_{CO}) can be given by eqs 5, 6, and 13

$$\frac{n_S{}^2\cdot\nu(n_S)}{\left([V_{O,T}] + [O_{O,T}] - \left[\frac{n_S{}^2\cdot\nu(n_S)}{K_i} + \nu(n_S)\right]\right)}\cdot p_{O_2}{}^{0.5} = \frac{k_{des} + k_{react}\cdot p_{CO}}{k_{ads}} \tag{14}$$

$$\nu(n_S) = [V_{O,ini}{}^{2+}] - \mu_1\sqrt{\ln\frac{n_B}{n_S}}, \qquad \mu_1 = \sqrt{\frac{\varepsilon_S kT\cdot n_B}{2q^2}}$$

In order to explore the effect of P_{O_2} on sensitivity, let us suppose that there are two chambers with different oxygen partial pressures $P^{\sigma}_{O_2}$ and $P^{\gamma}_{O_2}$. Here, assuming $P^{\sigma}_{O_2} > P^{\gamma}_{O_2}$, according to eq 14, when $P_{CO} = 0$, n^{σ}_{S0} is lower than n^{γ}_{S0}. As the CO concentration increases, the electron concentration of both will increase and the variation curves of the electron concentration to the CO concentration are shown in Figure 4. It is worth noting that the slope of the two curves cannot indicate the level of sensitivity. Actually, because n^{γ}_{S0} is greater

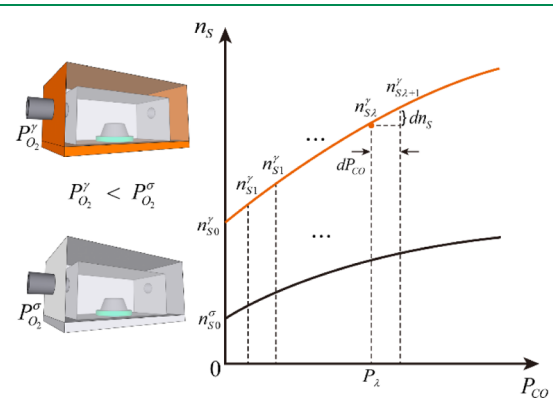

Figure 4. Variation of surface electron concentration on P_{CO} under different oxygen partial pressures $P^{\sigma}_{O_2}$ and $P^{\gamma}_{O_2}$, defining $P^{\sigma}_{O_2} > P^{\gamma}_{O_2}$.

https://doi.org/10.1021/acssensors.1c02753
ACS Sens. 2022, 7, 1095−1104

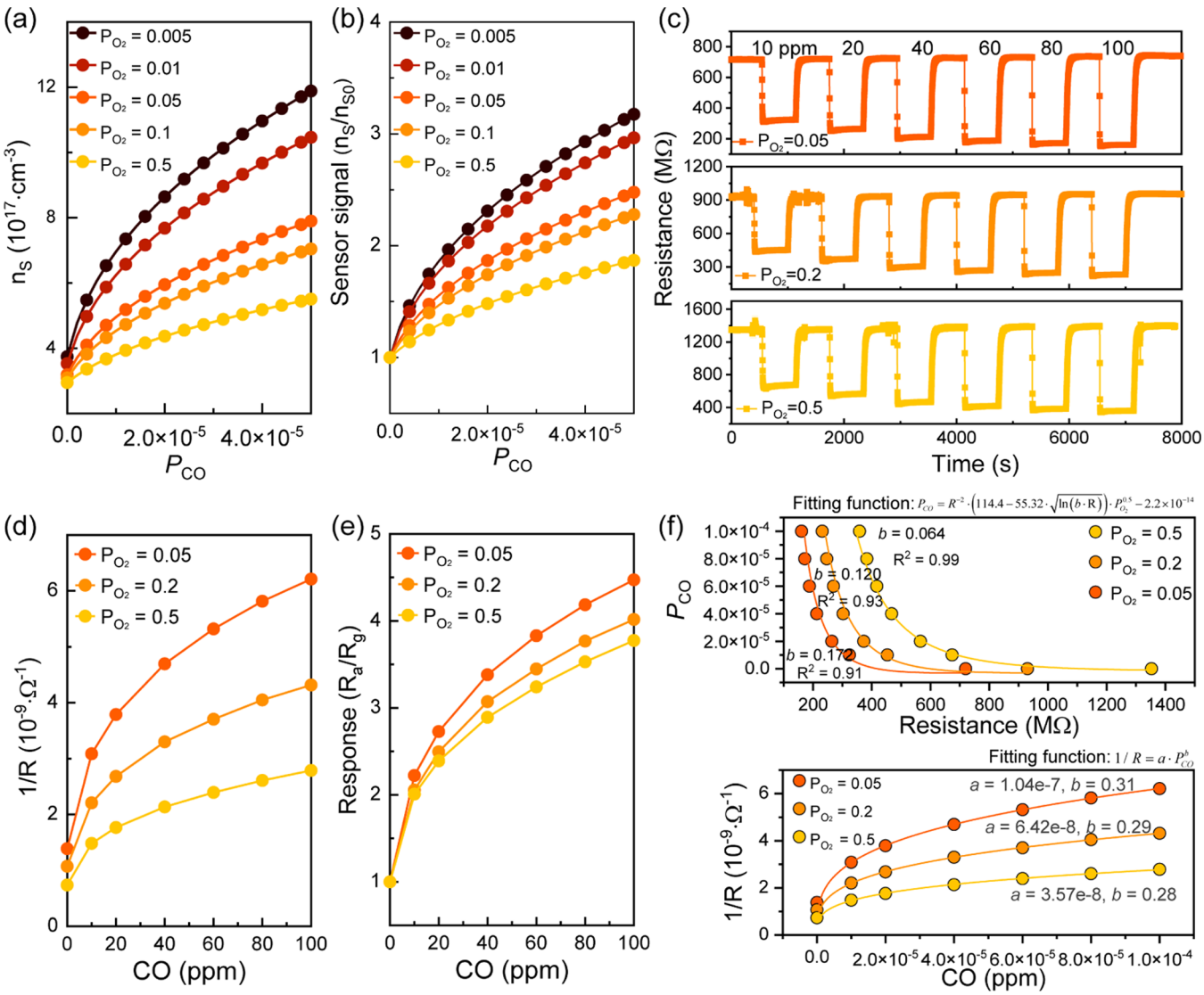

Figure 5. (a,b) Variation of the surface electron concentration (a) and response (b) as a function of P_{CO} with different oxygen partial pressure. (c) Dynamic resistance curve of the SnO_2-based sensor to CO gas in different oxygen backgrounds. (d, e) Variation of the reciprocal of resistance (d) and response (e) to CO gas in different oxygen backgrounds. (f) Fitting curves of resistance and CO concentration based on our model (eq 20) and traditional model ($G = a\cdot P_{CO}{}^{b}$).

than n_{S0}^{σ}. For a given CO concentration P_λ ($P_\lambda \neq 0$), even if $dn_{S\lambda}^{\gamma}/dP_\lambda$ is greater than $dn_{S\lambda}^{\sigma}/dP_\lambda$, it cannot be proved that $n_{S\lambda}^{\gamma}/n_{S0}^{\gamma}$ is greater than $n_{S\lambda}^{\sigma}/n_{S0}^{\sigma}$. However, one may divide the P_λ into infinite fragments. The gas response to P_λ is

$$S = \frac{n_{S\lambda}}{n_{S0}} = \frac{n_{S1}}{n_{S0}}\frac{n_{S2}}{n_{S1}}\frac{n_{S3}}{n_{S2}}\cdots\frac{n_{S\lambda-1}}{n_{S\lambda-2}}\frac{n_{S\lambda}}{n_{S\lambda-1}} \tag{15}$$

here, we define ds as

$$ds = \lim_{\Delta P_{CO}\to 0}\frac{n_{S\lambda+1}}{n_{S\lambda}} = \frac{n_S + \frac{dn_S}{dP_{CO}}\cdot dP_{CO}}{n_S} \tag{16}$$

Using eq 14, ds is given by

$$ds = \frac{k_{react}}{k_{des} + k_{react}\cdot P_{CO_\lambda}}g(n_{S\lambda})\cdot dP_{CO} + 1 \tag{17}$$

where

$$g(n_S) = \frac{[V_{O,T}] + [O_{O,T}] - \nu(n_S) - \frac{n_S{}^2\cdot\nu(n_S)}{K_i}}{2([V_{O,T}] + [O_{O,T}] - \nu(n_S)) + \frac{([V_{O,T}] + [O_{O,T}])\mu_1{}^2}{2\cdot\nu(n_S)\cdot[V_{O,ini}{}^{2+} - \nu(n_S)]}} \tag{18}$$

For the cases of the depletion region, it can be proved that $g(n_S)$ is an increasing function of n_S (see Note S3 and Figure S2 in the Supporting Information). For the case of $P_{O_2}^{\sigma} > P_{O_2}^{\gamma}$, because n_{S0}^{γ} is higher than n_{S0}^{σ} and ds is an increasing function of n_S, using eq 15 it can be proved that the sensor signal $S_\lambda^{\gamma} = n_{S\lambda}^{\gamma}/n_{S0}^{\gamma}$ is higher than $S_\lambda^{\sigma} = n_{S\lambda}^{\sigma}/n_{S0}^{\sigma}$.

According to the relevant experimental parameters reported in the previous literature,[10,32,33] we simulated the curves of n_S and sensor signal to various CO concentrations under different oxygen partial pressure, as shown in Figure 5a,b. Within the selected range of oxygen partial pressure, the response toward P_{CO} shows an increasing trend with decreasing P_{O_2}. However, this trend will be broken when the oxygen partial pressure continues to decrease, which causes the values of n_S and n_B to

https://doi.org/10.1021/acssensors.1c02753
ACS Sens. 2022, 7, 1095−1104

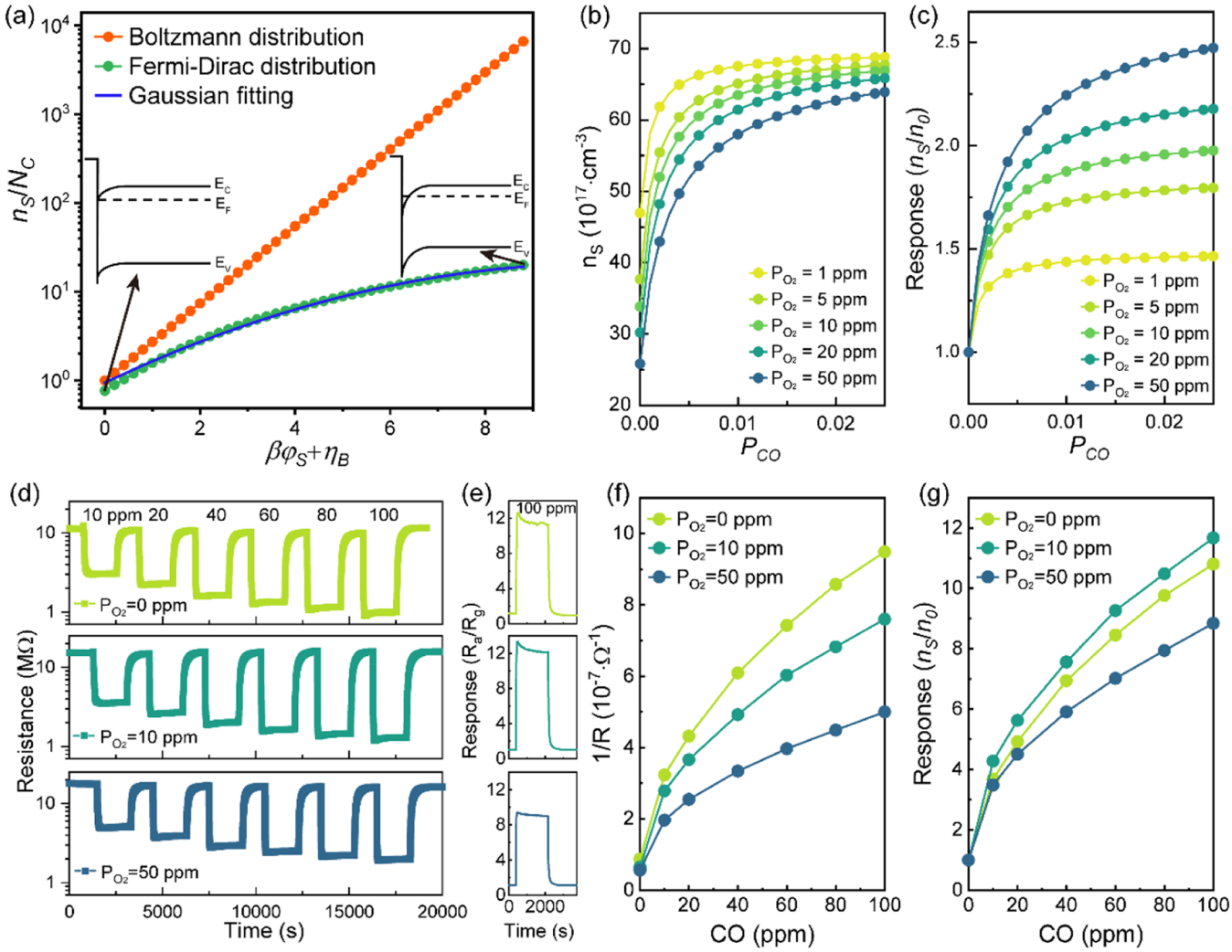

Figure 6. (a) Dependence of the electron concentration on band bending based on the Boltzmann distribution (orange) and Fermi−Dirac distribution (green) and the corresponding Gaussian fitting curve (blue). (b,c) Variation of surface electron concentration (b) and response (c) as a function of P_{CO} with different oxygen partial pressure. (d) Dynamic resistance curve of the SnO_2-based sensor to CO gases in different oxygen backgrounds. (e) Response curve of the SnO_2-based sensor to 100 ppm CO in different oxygen backgrounds. (f, g) Variation of the reciprocal of resistance (f) and response (g) to CO gases in different oxygen backgrounds.

be comparable (Figure S3). At this point, the depletion layer conditions will no longer be valid, and the error introduced by the Boltzmann distribution cannot be ignored, thus eq 14 fails to describe the dependence of the surface electron concentration on P_{O_2} and P_{CO}.

To further validate the accuracy of the model, the real-time responses of SnO_2-based sensor to CO gases (10−100 ppm) were measured at P_{O_2} = 0.05, 0.2, and 0.5, as shown in Figure 5c (the preparation method and TEM images of SnO_2 are shown in Note S4 and Figure S4 of the Supporting Information). As the oxygen partial pressure decreases, the baseline resistance of the sensor decreases from 1353 to 720 MΩ. However, the gas response to 100 ppm CO increases from 3.8 to 4.5 (Figure 5e). The result indicates that although the coverage of adsorbed oxygen on the SnO_2 surface decreases, the charge transfer caused by the CO oxidation increases instead. Figure 5d shows the curve of $1/R$ with the CO concentration, which is consistent with the curve of n_S with P_{CO} in Figure 5a. In the case of the depletion layer, given that the concentration of oxygen vacancies (the sum of ionized and unionized oxygen vacancies) $(n_S^2\cdot v(n_S)/K_i + v(n_S))$ is much lower than the total number of sites $([V_{O,T}] + [O_{O,T}])$. Equation 14 can be simplified as

$$P_{CO} = \frac{\frac{k_{ads}}{k_{react}}\cdot n_S^2\left([V_{O,ini}{}^{2+}] - \mu_1\sqrt{\ln\frac{n_B}{n_S}}\right)\cdot P_{O_2}{}^{0.5}}{([V_{O,T}] + [O_{O,T}]) - \frac{k_{ads}}{k_{react}}} \quad (19)$$

For the SnO_2 sensor, its resistance approximately depends on the reciprocal of the surface electron concentration (n_S), namely, $R \propto k/n_S$. Therefore, the resistance of the sensor, oxygen partial pressure and CO concentration obey the following equation

$$P_{CO} = R^{-2}[a - b\sqrt{\ln(c\cdot R)}]\cdot p_{O_2}{}^{0.5} - d \quad (20)$$

where, a, b, c, and d are theoretically constants. Based on eq 20, the resistance variation of the sensor to CO concentrations under different P_{O_2} are fitted, as shown in Figure 5f. With the decrease of P_{O_2}, the coefficient of determination (R^2) gradually decreases but all exceed 0.90, suggesting the high goodness-of-

https://doi.org/10.1021/acssensors.1c02753
ACS Sens. 2022, 7, 1095−1104

fit. However, it is found that only three parameters (a, b, and d) can remain constant while the parameter c increases with the decrease of P_{O_2}. The underlying reason can be attributed to the fact that the depletion layer conditions become unreliable with decreasing oxygen partial pressure and increasing CO concentration, which causes the Boltzmann distribution to not describe the surface electron concentration very well. Comparing with the traditional model function: $G = a \cdot P_{CO}{}^{b}$ (Figure 5f),[8] the number of parameters that vary with oxygen partial pressure in our model is reduced to one. This will greatly reduce the effort required to calibrate these variable parameters in applications. Furthermore, we also perform the fit analysis for the dependence of resistance on oxygen partial pressure at constant CO concentrations of 10 and 50 ppm (see Note S5 and Figures S5 and S6 in the Supporting Information). Likewise, it is found that the fitting curves gradually deviate from the measured resistance with the decrease of oxygen partial pressure. Moreover, the coefficient of determination of the fitting curve at a CO concentration of 50 ppm is lower than that of the fitting curve at a CO concentration of 10 ppm.

Accumulation Layer. When the P_{O_2} in the background atmosphere is quite low or the concentration of the reducing gas is sufficiently high, the energy band will bend downward, leading to the Fermi level E_F approaching or entering the conduction band E_C. The Boltzmann distribution is not valid anymore. The Fermi−Dirac integral distribution should be adopted to describe the surface electron concentration

$$n = \int_{E_C}^{\infty} f(E) N_C(E)\, \mathrm{d}E = \frac{4\pi(2m_{dn})^{3/2}}{h^3} \int_{E_C}^{\infty} \frac{(E - E_C)^{1/2}}{\exp\left(\frac{E - E_C - (E_F - E_C)_B}{KT}\right) + 1}\, \mathrm{d}E \tag{21}$$

According to eq 21, the value of n_S can be obtained using the Fermi−Dirac integral after acquiring the values of $(E_F - E_C)_B$ and band bending $q\varphi_S$. However, this infinite integral restricts the subsequent mathematical derivation. Here, combined with previous experiments on the band bending of SnO_2 in gas detection,[34] the Fermi−Dirac distribution is fitted with the Gaussian function. The lower limit of band bending is set to the position where the conduction band bends down to the Fermi energy level at the surface (the Boltzmann distribution is surely not valid), and the upper limit of the band bending is set to the position where the conduction band crosses the Fermi energy level and further bends downward by 0.4 eV, as shown in Figure 6a. In this interval, the distribution of electrons can be described by the following Gaussian function

$$\frac{n_S}{N_C} = 20.95 \cdot \exp\left[-\left(\frac{\beta\varphi_S + \eta_B - 10.6}{6.02}\right)^2\right] \tag{22}$$

$$\eta_B = \left(\frac{E_F - E_c}{KT}\right)_B$$

The relationship between n_S and the gas partial pressure (P_{O_2} and p_{CO}) can be given by eqs 5, 6, and 22.

$$\frac{n_S{}^2 \cdot \nu(n_S)}{\left([V_{O,T}] + [O_{O,T}] - \left[\frac{n_S{}^2 \cdot \nu(n_S)}{K_i} + \nu(n_S)\right]\right)} \cdot p_{O_2}{}^{1/2} = \frac{k_{des} + k_{react} \cdot p_{CO}}{k_{ads}} \tag{23}$$

$$\nu(n_S) = [V_{O,ini}{}^{+}] + \mu_2 \cdot \exp\left(-3.01 \cdot \sqrt{\ln \frac{20.95 \cdot N_C}{n_S}}\right),$$

$$\mu_2 = \frac{\sqrt{2}\, \varepsilon_S kT}{2q^2 L_D} \cdot e^{10.6 - \eta_B/2}$$

Using eq 23, ds is given by

$$\mathrm{d}s = \frac{k_{react}}{k_{des} + k_{react} \cdot P_{CO_\lambda}} g(n_{S\lambda}) \cdot \mathrm{d}P_{CO} + 1 \tag{24}$$

where

$$g(n_S) = \left\{[V_{O,T}] + [O_{O,T}] - \nu(n_S) - \frac{n_S{}^2 \cdot \nu(n_S)}{K_i}\right\} \Big/ \left\{2 \cdot ([V_{O,T}] + [O_{O,T}] - \nu(n_S)) + \frac{3.01 \cdot ([V_{O,T}] + [O_{O,T}]) \cdot (\nu(n_S) - V_{O,ini}{}^{2+})}{2 \cdot (\nu(n_S) \cdot \sqrt{\ln(20.95 \cdot N_C/n_S)}}\right\} \tag{25}$$

Different from the case of the depletion layer, $g(n_s)$ in the accumulation region is a monotonically decreasing function of n_S, which indicates that the sensor signal will definitely decrease with the decrease of P_{O_2} once the conduction band bends downward into the Fermi level (the detailed monotonicity derivation is presented in Note S6 of the Supporting Information). According to eq 23, the curves of the surface electron concentration and sensor signal to the CO concentration under different oxygen partial pressures are simulated, as shown in Figure 6b,c. The Fermi−Dirac distribution extremely slows down the increase of the electron concentration with the increase of P_{CO}, which causes the sensing signal to exhibit a typical saturation phenomenon, and the sensing signal tends to saturate more easily as P_{O_2} decreases. Within the selected range of oxygen partial pressure, the sensor signal gradually approaches 1 with the decrease of oxygen partial pressure. Therefore, although the numerical solution cannot be obtained by eq 23 for the case of $P_{O_2} = 0$, the sensor signal should drop to 1 according to the physical definition of the model. After oxygen desorption or CO oxidation, the absence of oxygen will prevent the formation of newly adsorbed oxygen, which leaves the surface ultimately free of oxygen species that participate in CO oxidation. Therefore, the surface electron concentration will no longer vary with the CO concentration when $P_{O_2} = 0$. Combining the function models under the depletion and accumulation layers, the effect of oxygen partial pressure on the CO sensing of the SnO_2-based sensor is that the response of the SnO_2 sensor to CO will first increase and then decrease with the increase of P_{O_2}. However, previous experiments only observed a decrease in the CO response with increasing oxygen concentration,

https://doi.org/10.1021/acssensors.1c02753
ACS Sens. 2022, 7, 1095−1104

which indicates that an extremely low oxygen partial pressure is required for the formation of the accumulation layer on the surface.

Drawn from the above discussion, a high purity N_2 gas (99.9999%) and a 100 ppm O_2/N_2 mixed gas were selected to prepare different concentrations of hypoxic atmospheres (0, 10, and 50 ppm O_2) and the CO responses of SnO_2-based sensors in these atmospheres are tested, as shown in Figure 6d. Due to the hypoxic atmospheres, the recovery time of the sensor increases from ~55 s (P_{O_2} = 0.05) to 530−1200 s (P_{O_2} = 0). The results suggest that there is still a trace of oxygen in the test system, even with high purity N_2 gas, which allows the resistance of the sensor to slowly return to the baseline resistance. Besides, the dynamic response curves of the SnO_2 sensor to 100 ppm CO are shown in Figure 6e. For P_{O_2} = 0 and 10 ppm, the response curves have a clear spike and take a long time to stabilize, and this phenomenon is not apparent at low concentrations of CO (Figure S7). The possible reason is that in the recovery process, the oxygen molecules will be adsorbed and dissociate on the SnO_2 surface and slowly reach saturation and in the CO detection process, the oxidation of CO will produce a large number of oxygen vacancies at the beginning, while these vacancies cannot be healed in time due to the trace amount of oxygen. Therefore, a longer time is required for the response curve to reach equilibrium. Figure 6f,g shows the changes of the resistance and responses to various CO concentration under different P_{O_2}. As the oxygen concentration increases from 0 to 10 ppm, the CO response of the SnO_2 sensor will have an increase but rapidly decreases with the further increase in the oxygen concentration, which is consistent with the prediction of our model.

Vicinity of the Flat Band. This case can be described mathematically as the neighborhood of $\varphi_S = 0$, which is not a region like the depletion layer or the accumulation layer but a point. The function model in this neighborhood provides further understanding of the variation of sensitivity with oxygen partial pressure. Using the different SnO_2 preparation processes, the value of $(E_C - E_F)_B$ varies widely. Here, we assume that the Boltzmann distribution is still valid in the vicinity of the flat band. The concentration of ionized oxygen vacancy can be obtained by eqs 7, 11, and 12

$$v(n_S) = [V_{O,ini}{}^{2+}] + \mu_3 \cdot \ln \frac{n_S}{n_B}, \qquad \mu_3 = \frac{\varepsilon_S KT}{2q^2 L_D}$$

and the $g(n_S)$ is given using the same method

$$g(n_S) = \frac{[V_{O,T}] + [O_{O,T}] - v(n_S) - \frac{n_S{}^2 \cdot v(n_S)}{K_i}}{2([V_{O,T}] + [O_{O,T}] - v(n_S)) + \frac{([V_{O,T}] + [O_{O,T}])\mu_3}{v(n_S)}}$$

The monotonicity of $g(n_S)$ depends on the value of $[V_{O,ini}{}^{2+}]$. When $[V_{O,ini}{}^{2+}] \ll [V_{O,T}] + [O_{O,T}]$, meaning a large $(E_C - E_F)_B$, the $g(n_S)$ is an increasing function of n_S, as shown in Figure 7a, and the $g(n_S)$ will change from increasing function to decreasing function with a value of $[V_{O,ini}{}^{2+}]$ approaching $[V_{O,T}] + [O_{O,T}]$ (Figure 7b,c). Combining the monotonicity of the $g(n_S)$ in the depletion and accumulation layers, it can be concluded that for a SnO_2-based sensor with a lower work function (behave with a low resistance), it will easily reach the accumulation case discussed above when the band bends downward. The $g(n_S)$ is a decreasing function in the vicinity of the flat band and accumulation layers. For a

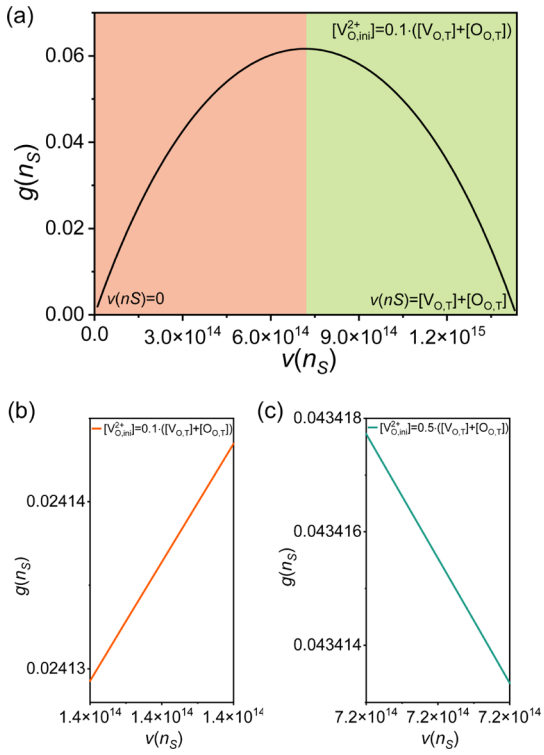

Figure 7. (a) Function curve of $g(n_S)$ in the interval of (0, $[V_{O,T}]$ + $[O_{O,T}]$). (b, c) Monotonicity of $g(n_S)$ in the neighborhood of $\varphi = 0$ with different values of $[V_{O,ini}{}^{2+}]$.

SnO_2 sensor with a higher work function (behave with a high resistance), the large value of $(E_C - E_F)_B$ makes $g(n_S)$ still an increasing function in the vicinity of the flat band and needs quite a downward band bending to reach the accumulation case.

CONCLUSIONS

In summary, on the basis of the reported experiment and theoretical research of SnO_2, we build a sensing reaction model to explain the effect of oxygen partial pressure on the sensitivity of a SnO_2-based sensor. In the case of the depletion layer, the model provides a good description of the relationship between the sensor resistance, oxygen partial pressure, and target gas, which facilitates the calibration of sensitivity for applications with oxygen partial pressure variation. The increasing trend of gas response with decreasing oxygen partial pressure demonstrates a unique perspective that reducing oxygen adsorption will instead improve the gas performance, which provides an innovative ideation for the design of a high-performance sensor. Besides, based on the model in the accumulation layer, we find a new phenomenon that the sensitivity of SnO_2 decreases with the decrease of oxygen partial pressure in an extremely hypoxic atmosphere, which indicates that the sensor signal cannot keep increasing with decreasing partial pressure of oxygen.

ASSOCIATED CONTENT

Supporting Information

The Supporting Information is available free of charge at https://pubs.acs.org/doi/10.1021/acssensors.1c02753.

Computational details for DFT calculations, resistance curve of the SnO_2 sensor in air and CO_2 gas, derivation

https://doi.org/10.1021/acssensors.1c02753
ACS Sens. 2022, 7, 1095−1104

of the space charge per unit area Q_S, monotonicity derivation of $g(n_S)$ in the case of the depletion layer, an illustration of the increasing trend of the sensor signal on the oxygen partial pressure being broken when the values of n_{S0} and n_B are comparable, synthesis of SnO_2 nanoparticles and their TEM image, fit analysis for the dependence of resistance on the oxygen partial pressure at a constant CO pressure, monotonicity derivation of $g(n_S)$ in the case of the accumulation layer, dynamic CO response curve of the SnO_2-based sensor in different hypoxic atmospheres, and MATLAB code for simulation of the surface electron concentration and sensor signal curves (PDF)

AUTHOR INFORMATION

Corresponding Authors

Peng Sun − *State Laboratory on Integrated Optoelectronics, College of Electronic Science and Engineering, Jilin University, Changchun 130012, China;* orcid.org/0000-0002-9509-9431; Email: pengsun@jlu.edu.cn

Geyu Lu − *State Laboratory on Integrated Optoelectronics, College of Electronic Science and Engineering, Jilin University, Changchun 130012, China;* orcid.org/0000-0002-7428-2456; Email: lugy@jlu.edu.cn

Authors

Liupeng Zhao − *State Laboratory on Integrated Optoelectronics, College of Electronic Science and Engineering, Jilin University, Changchun 130012, China*

Xueqin Gong − *State Laboratory on Integrated Optoelectronics, College of Electronic Science and Engineering, Jilin University, Changchun 130012, China*

Wei Tao − *State Laboratory on Integrated Optoelectronics, College of Electronic Science and Engineering, Jilin University, Changchun 130012, China*

Tianshuang Wang − *State Laboratory on Integrated Optoelectronics, College of Electronic Science and Engineering, Jilin University, Changchun 130012, China;* orcid.org/0000-0003-3196-3005

Fangmeng Liu − *State Laboratory on Integrated Optoelectronics, College of Electronic Science and Engineering, Jilin University, Changchun 130012, China;* orcid.org/0000-0002-5555-5543

Xishuang Liang − *State Laboratory on Integrated Optoelectronics, College of Electronic Science and Engineering, Jilin University, Changchun 130012, China*

Fengmin Liu − *State Laboratory on Integrated Optoelectronics, College of Electronic Science and Engineering, Jilin University, Changchun 130012, China;* orcid.org/0000-0003-1523-2915

Yanchao Wang − *State Key Laboratory of Superhard Materials and International Center of Computational Method and Software, College of Physics, Jilin University, Changchun 130012, China;* orcid.org/0000-0003-4518-925X

Complete contact information is available at: https://pubs.acs.org/10.1021/acssensors.1c02753

Notes

The authors declare no competing financial interest.

ACKNOWLEDGMENTS

This work was supported by the National Nature Science Foundation of China (nos. 61833006 and 61831011), Jilin Province Science and Technology Development Plan Program (no. 20200301010RQ), Project on Industrial Innovation Capability of Jilin Province (no. 2020C048), and Fundamental Research Funds for the Central Universities and Graduate Interdisciplinary Research Fund of Jilin University (no. 10183201833).

REFERENCES

(1) Suematsu, K.; Hiroyama, Y.; Harano, W.; Mizukami, W.; Watanabe, K.; Shimanoe, K. Double-Step Modulation of the Pulse-Driven Mode for a High-Performance SnO_2 Micro Gas Sensor: Designing the Particle Surface via a Rapid Preheating Process. *ACS Sens.* **2020**, *5*, 3449−3456.

(2) Jeong, H.-M.; Kim, J.-H.; Jeong, S.-Y.; Kwak, C.-H.; Lee, J.-H. Co_3O_4−SnO_2 Hollow Heteronanostructures: Facile Control of Gas Selectivity by Compositional Tuning of Sensing Materials via Galvanic Replacement. *ACS Appl. Mater. Interfaces* **2016**, *8*, 7877−7883.

(3) Jang, J.-S.; Yu, S.; Choi, S.-J.; Kim, S.-J.; Koo, W.-T.; Kim, I.-D. Metal Chelation Assisted In Situ Migration and Functionalization of Catalysts on Peapod-Like Hollow SnO_2 toward a Superior Chemical Sensor. *Small* **2016**, *12*, 5989−5997.

(4) Suman, P. H.; Felix, A. A.; Tuller, H. L.; Varela, J. A.; Orlandi, M. O. Comparative gas sensor response of SnO_2, SnO and Sn_3O_4 nanobelts to NO_2 and potential interferents. *Sens. Actuators, B* **2015**, *208*, 122−127.

(5) Liu, X.; Chen, N.; Han, B.; Xiao, X.; Chen, G.; Djerdj, I.; Wang, Y. Nanoparticle cluster gas sensor: Pt activated SnO_2 nanoparticles for NH_3 detection with ultrahigh sensitivity. *Nanoscale* **2015**, *7*, 14872−14880.

(6) Grossmann, K.; Wicker, S.; Weimar, U.; Barsan, N. Impact of Pt additives on the surface reactions between SnO_2, water vapour, CO and H_2; an operando investigation. *Phys. Chem. Chem. Phys.* **2013**, *15*, 19151−19158.

(7) Yamazoe, N.; Sakai, G.; Shimanoe, K. Oxide semiconductor gas sensors. *Catal. Surv. Asia* **2003**, *7*, 63−75.

(8) Barsan, N.; Weimar, U. Conduction model of metal oxide gas sensors. *J. Electroceram.* **2001**, *7*, 143−167.

(9) Schmid, W.; Bârsan, N.; Weimar, U. Sensing of hydrocarbons and CO in low oxygen conditions with tin dioxide sensors: possible conversion paths. *Sens. Actuators, B* **2004**, *103*, 362−368.

(10) Bârsan, N.; Hübner, M.; Weimar, U. Conduction mechanisms in SnO_2 based polycrystalline thick film gas sensors exposed to CO and H_2 in different oxygen backgrounds. *Sens. Actuators, B* **2011**, *157*, 510−517.

(11) Van den Schoor, F.; Norman, F.; Vandermeiren, K.; Verplaetsen, F.; Berghmans, J.; Van den Bulck, E. Flammability limits, limiting oxygen concentration and minimum inert gas/combustible ratio of H_2/CO/N_2/air mixtures. *Int. J. Hydrogen Energy* **2009**, *34*, 2069−2075.

(12) Itoh, T.; Izu, N.; Tsuruta, A.; Akamatsu, T.; Shin, W.; Kamihoriuchi, K.; Takizawa, M.; Yoshida, I. Effect of Pt electrodes in cerium oxide semiconductor-type oxygen sensors evaluated using alternating current. *Sens. Actuators, B* **2021**, *345*, 130396.

(13) Degler, D.; Wicker, S.; Weimar, U.; Barsan, N. Identifying the Active Oxygen Species in SnO_2 Based Gas Sensing Materials: An Operando IR Spectrsocopy Study. *J. Phys. Chem. C* **2015**, *119*, 11792−11799.

(14) Yamazoe, N.; Fuchigami, J.; Kishikawa, M.; Seiyama, T. Interactions of tin oxide surface with O_2, H_2O AND H_2. *Surf. Sci.* **1979**, *86*, 335−344.

(15) Hua, Z.; Qiu, Z.; Li, Y.; Zeng, Y.; Wu, Y.; Tian, X.; Wang, M.; Li, E. A theoretical investigation of the power-law response of metal

oxide semiconductor gas sensors II: Size and shape effects. *Sens. Actuators, B* **2018**, *255*, 3541−3549.
(16) Hua, Z.; Li, Y.; Zeng, Y.; Wu, Y. A theoretical investigation of the power-law response of metal oxide semiconductor gas sensors I: Schottky barrier control. *Sens. Actuators, B* **2018**, *255*, 1911−1919.
(17) Oviedo, J.; Gillan, M. J. First-principles study of the interaction of oxygen with the SnO_2(110) surface. *Surf. Sci.* **2001**, *490*, 221−236.
(18) Gurlo, A. Interplay between O_2 and SnO_2: Oxygen Ionosorption and Spectroscopic Evidence for Adsorbed Oxygen. *ChemPhysChem* **2006**, *7*, 2041−2052.
(19) Sopiha, K. V.; Malyi, O. I.; Persson, C.; Wu, P. Chemistry of Oxygen Ionosorption on SnO_2 Surfaces. *ACS Appl. Mater. Interfaces* **2021**, *13*, 33664−33676.
(20) Merte, L. R.; Jørgensen, M. S.; Pussi, K.; Gustafson, J.; Shipilin, M.; Schaefer, A.; Zhang, C.; Rawle, J.; Nicklin, C.; Thornton, G.; et al. Structure of the SnO_2(110)−(4×1) Surface. *Phys. Rev. Lett.* **2017**, *119*, 096102.
(21) Li, G.; Li, S.; Han, Z.-K.; Zou, C.; Wu, H.; Yuan, W.; Zhu, B.; Gao, Y.; Yang, H.; Zhang, Z.; et al. In Situ Resolving the Atomic Reconstruction of SnO_2(110) Surface. *Nano Lett.* **2021**, *21*, 7309−7316.
(22) Emiroglu, S.; Bârsan, N.; Weimar, U.; Hoffmann, V. In situ diffuse reflectance infrared spectroscopy study of CO adsorption on SnO_2. *Thin Solid Films* **2001**, *391*, 176−185.
(23) Chen, K.; Zhou, Y.; Jin, R.; Wang, T.; Liu, F.; Wang, C.; Yan, X.; Sun, P.; Lu, G. Gas sensor based on cobalt-doped 3D inverse opal SnO_2 for air quality monitoring. *Sens. Actuators, B* **2022**, *350*, 130807.
(24) Degler, D.; Müller, S. A.; Doronkin, D. E.; Wang, D.; Grunwaldt, J.-D.; Weimar, U.; Barsan, N. Platinum loaded tin dioxide: a model system for unravelling the interplay between heterogeneous catalysis and gas sensing. *J. Mater. Chem. A* **2018**, *6*, 2034−2046.
(25) Singh, A. K.; Janotti, A.; Scheffler, M.; Van de Walle, C. G. Sources of Electrical Conductivity in SnO_2. *Phys. Rev. Lett.* **2008**, *101*, 055502.
(26) Kılıç, Ç.; Zunger, A. Origins of Coexistence of Conductivity and Transparency in SnO_2. *Phys. Rev. Lett.* **2002**, *88*, 095501.
(27) Ágoston, P.; Albe, K.; Nieminen, R. M.; Puska, M. J. Intrinsicn-Type Behavior in Transparent Conducting Oxides: A Comparative Hybrid-Functional Study of In_2O_3, SnO_2, and ZnO. *Phys. Rev. Lett.* **2009**, *103*, 245501.
(28) Yamaguchi, Y.; Nagasawa, Y.; Tabata, K.; Suzuki, E. The Interaction of Oxygen with Reduced SnO_2 and Ti/SnO_2 (110) Surfaces: A Density Functional Theory Study. *J. Phys. Chem. A* **2001**, *106*, 411−418.
(29) Samson, S.; Fonstad, C. G. Defect structure and electronic donor levels in stannic oxide crystals. *J. Appl. Phys.* **1973**, *44*, 4618−4621.
(30) Elger, A. K.; Hess, C. Elucidating the Mechanism of Working SnO_2 Gas Sensors Using Combined Operando UV/Vis, Raman, and IR Spectroscopy. *Angew. Chem., Int. Ed.* **2019**, *58*, 15057−15061.
(31) Elger, A. K.; Hess, C. Application of Raman Spectroscopy to Working Gas Sensors: From in situ to operando Studies. *Sensors* **2019**, *19*, 5075.
(32) Oprea, A.; Moretton, E.; Bârsan, N.; Becker, W. J.; Wöllenstein, J.; Weimar, U. Conduction model of SnO_2 thin films based on conductance and Hall effect measurements. *J. Appl. Phys.* **2006**, *100*, 033716.
(33) Oprea, A.; Bârsan, N.; Weimar, U. Characterization of granular metal oxide semiconductor gas sensitive layers by using Hall effect based approaches. *J. Phys. D: Appl. Phys.* **2007**, *40*, 7217−7237.
(34) Hübner, M.; Bârsan, N.; Weimar, U. Influences of Al, Pd and Pt additives on the conduction mechanism as well as the surface and bulk properties of SnO_2 based polycrystalline thick film gas sensors. *Sens. Actuators, B* **2012**, *171−172*, 172−180.

Recommended by ACS

In Operando Investigation of the Concentration Dependent NO_2 Sensing Mechanism of Bi_2S_3 Nanorods at Low Temperatures and the Interference of O_3

Tamara Russ, Nicolae Barsan, *et al.*
OCTOBER 06, 2022
ACS SENSORS
READ

Ultrasensitive Formaldehyde Sensor Based on SnO_2 with Rich Adsorbed Oxygen Derived from a Metal Organic Framework

Zongming Deng, Qingju Liu, *et al.*
SEPTEMBER 01, 2022
ACS SENSORS
READ

Promoted Carbon Monoxide Sensing Performance of a $Bi_2Mn_4O_{10}$-Based Mixed-Potential Sensor by Regulating Oxygen Vacancies

Hongming Liu, Jianzhong Xiao, *et al.*
SEPTEMBER 27, 2022
ACS SENSORS
READ

Nanostructured SnO_2 Microsphere-Based Gas Sensor Array Enhanced by Molecular Imprinting for Methanol and Ethanol Discriminative Detection

Weinan Song, Shuang Yan, *et al.*
SEPTEMBER 12, 2022
ACS APPLIED NANO MATERIALS
READ

Get More Suggestions >

https://doi.org/10.1021/acssensors.1c02753
ACS Sens. 2022, 7, 1095−1104